The International Journal of Advanced Manufacturing Technology (2019) 103:943–955
https://doi.org/10.1007/s00170-019-03547-y

ORIGINAL ARTICLE

Mechanical and tribological assessments of high-vanadium high-speed steel by the conventional powder metallurgy process

Shanhong Wan[1] · Huan Li[2] · Kiet Tieu[1] · Qi Xue[2] · Hongtao Zhu[1]

Received: 31 August 2018 / Accepted: 4 March 2019 / Published online: 27 March 2019
© Springer-Verlag London Ltd., part of Springer Nature 2019

Abstract

This paper reported the facile fabrication of high-vanadium high-speed steel (HVHSS) by the conventional powder metallurgy process for the wear-resistant applications. The effect of compaction pressure and of subsequent sintering temperatures on the formability and structural evolution of HVHSS was assessed by scanning electron microscopy (SEM) with electron-dispersive spectra (EDS), and X-ray diffraction (XRD) analysis. The results well revealed the primary constitution composed of mixed hardening phases MC and M_6C existing within the α-ferrite matrix after hot solidification, and the association of microstructural alteration with the sintering temperatures was discussed for as-obtained HVHSS specimens. The HVHSS attained the desirable values of mechanical hardness and bending strength and thereby delivered the capability of friction reduction and wear inhibition, closely depending on the sintering temperature. The optimal sintering condition was determined on the basis of bulk density, shrinkage, and capability assessments. A well-established fabricating route for producing high-quality HVHSS was explored through the combined process of cold compaction and subsequent sintering on the conceptual design of chemical composition and alloying design of commercial M2 steel.

Keywords Powder metallurgy · High-vanadium high-speed steel · Microstructure · Sintering temperature · Friction and wear · Mechanical property

1 Introduction

To fulfil ever-increasing demands in high-strength steel manufacturing processes, the pursuit of innovative steel-based tool materials with superiority of wearing durability and operational stability has been continuous to assure the reliable operation of advanced manufacturing processing and the quality of ultimate products. High-speed steel (HSS) demonstrates the unique properties of abrasion resistance and thermal strength coupled with appreciable hot hardness, which have been applied as the tool material and wear-resistant parts [1–4]. Different from the mechanical and wear-resistant capabilities of aluminum alloys only applicable at room/ambient temperatures [5–9], HSS can be applicable to be the work rolls as the finishing stands of hot rolling sector especially submitted to the harsh ambiences, due to the excellent thermo-mechanical strength and exceptional toughness of bulk [10–13].

From the compositional and structural view, HSS is a typical metallic matrix composite (MMC) made of a ferrous matrix with the hardening inclusions such as ceramic carbides, in which the main alloying elements are chromium, vanadium, molybdenum, and tungsten in equilibrium with carbon [1]. Recent research towards high-speed steel is the simultaneous increment of vanadium and carbon with reducing the tungsten concentration, as service lives of such HSS is three times longer than that of high chromium cast iron and ten times longer than that of high manganese steel [14]. Such type of HSS contains higher amount of vanadium (9~10 wt%) and carbon (3~3.4 wt%), which are beneficial to refine the eutectic carbides of the M_2C and M_7C_3 types through forming fine and globular MC particles due to the well-dispersed hard VC carbides, which eventually promote the strength and toughness against abrasion and impact at elevated temperatures [14–17]

✉ Kiet Tieu
ktieu@uow.edu.au

✉ Qi Xue
qxue01@163.com

[1] Faculty of Engineering and Information Sciences, University of Wollongong, Wollongong 2522, Australia

[2] School of Materials Science and Engineering, Southwest Petroleum University, Chengdu 610500, People's Republic of China

and prolong the work roll substantially [18]. Furthermore, higher amount of vanadium improves the tribological durability and adaptability evaluation simultaneously by the favorable lubricity due to vanadium oxide at rubbing interface [18, 19].

The typical composition of eutectic carbides within the M2 steel is summarized in Table 1. The M2 steel generally contains 1.5~2.5 wt% C, up to 6 wt% W, up to 6 wt% Mo, 3–8 wt% Cr, and 4–10 wt% V. An empirical value of 4 wt% for chromium carbide ensures strength and toughness at the right balance [16]. Another primary alloying element is molybdenum with the content of 3~8 wt%, which can improve the hardenability by lowering the critical cooling rate. Molybdenum forms the cemented carbides as tungsten does since it has about half the atomic weight of tungsten, 1% Mo being used to replace 2% W. Molybdenum has a relatively lower melting point as compared with tungsten. Because of shortage of W together with complex heating processing techniques, the use of Mo to replace W became fairly common in the manufacturing HSS. In this study, part of Mo_2C was applicable as the candidate of WC.

High concentrations of vanadium and carbon additions promote the wear prevention significantly in comparison with the normal HSS [14, 18]. Note that the concentration of carbon within iron matrix is totally 1.5~2.5 wt%, while the carbon inclusion within the iron matrix rather than that of eutectic carbides in the range of 0.3~0.6 wt% specifically gives the substantial contribution to wear resistance, red hardness, and compressive strength [20]. If quantity of carbon is in excess of 0.6 wt%, a large amount of mixed austenite and lamellar martensite is retained and as a result, the comprehensively mechanical capability of steel deteriorated [17]. The excessive addition of vanadium and carbon thus impairs the hot workability [21]. So a critical value of additional carbon (0.6 wt%) is selected and further justified in the experimental section.

Various types of alloying carbides presenting within the iron matrix are harder than that of cementite and martensite of steel and thus enable the superior capability against impact and fracture during hot manufacturing operations [18, 19, 22, 23]. Thus, the final performance of HSS strongly relates to the balanced composition of carbon and alloy constituents within the iron matrix in terms of the deliberate content, morphology, and particle size distribution of carbides, where the hard phases of M_6C, M_2C, M_3C_7, and MC eutectic carbides contribute substantially to the mechanical reinforcement and wear mitigation [15, 22]. However, coarse carbides and consequent formation of large carbide networks during sintering process often lead to the detrimental stress accumulation and more brittleness that promotes crack initiation readily, which fatally undermines the toughness of HSS [24, 25].

In an effort to reduce the complexity of PM manufacturing and to improve tribological adaptability, a facile fabrication was proposed to develop HVHSS on the basis of alloying composite and metallographic composition of commercially M2 steel, where part of Mo_2C is used as the replacement of WC and high vanadium carbide presented in this powder formulation. The overall aim of this study was to develop the well-established program of compaction and sintering for the reliable production of HVHSS through the conventional powder metallurgy route. The structural verification and the mechanical hardness, fracture toughness, and tribological capabilities were performed for developing HVHSS in this study.

Table 1 Primary carbides and corresponding carbon content of M2 steel (wt%)

Carbide	W_2C	WC	Mo_2C	Fe_3Mo_3C	Cr_7C_3
Carbon content (%)	0.0316	0.0613	0.0591	0.0257	0.0900
Carbide	Cr_3C_2	$Cr_{23}C_6$	Fe_3Cr_3C	VC	
Carbon content (%)	0.1333	0.0568	0.0358	0.1907	

Source: [16]

2 Experimental details

2.1 Materials

The main raw materials listed in Table 2 were supplied by Chengdu Chemical Reagent Manufacturer in China. According to the alloying concept of proposed HVHSS, the weight proportion of mixed powders is given in Table 2, which were further weighed for mixing powders by the electronic analytical balance with a resolution of 0.00 01 g. An addition of 0.5 wt% carbon in the form of graphite powder (< 5 μm) was added to improve the sintering availability of the HVHSS materials, which was ascertained and justified from the following calculation. After wet milling process, the mean particle size was around 6 μm.

Within the M2 steel, the content of Cr, Mo, and V should be 4 wt%, 5 wt%, and 5 wt%, respectively. On the concepts of the alloying strategy and eutectic carbide composition within the HSS matrix, carbide powders were utilized directly as the pristine powders instead of metallic Cr, Mo, and V. The primarily eutectic carbides and respective carbon content (wt%) within HVHSS are found in Table 1. As Mo and C form Mo_2C, several types of chromium carbides exist such as

Table 2 Elemental composition of proposed HVHSS

	Mo	Cr	V	C	Fe
Concentration (wt%)	5	4	5	2.6	83.4
The weight concentration of mixed powders for fabricating HVHSS					
	Mo_2C	Cr_3C_2	VC	C	Fe
Concentration (wt%)	5.3140	4.6152	6.1782	0.5	83.4

Cr_7C_3, Cr_3C_2, $Cr_{23}C_6$, and $(Fe, Cr)_6C$. Normally, $(Fe, Cr)_6C$, also namely Fe_3Cr_3C, accounts for 50%, while Cr_7C_3, Cr_3C_2, and $Cr_{23}C_6$ represent the other 50% [16]. Moreover, Fe further accounts for 85% of C amount with higher concentration of martensite, equal to 0.51%; the carbon content within the steel matrix was assessed according to the empirical formula:

$$\begin{aligned} w\,(C) &= 0.0646w\,(Cr) + 0.0591w\,(Mo) + 0.1907w\,(V) \\ &\quad + 0.5 \\ &= 1.507 + 0.5 = 2.007 \end{aligned}$$

Accordingly, the chemical composition of HVHSS and corresponding percentage of raw powder materials in this study is shown in Table 2. Generally, HVHSS obtained from the conventional PM route usually contains about 15% undissolved carbides and about 15–30% untransformed austenite [21]. The subsequent quenching and tempering processes are necessarily required to render the martensite softening and to yield more precipitation of eutectic carbides [26]. In this study, the optimization of pore free HVHSS was mainly considered with respect to the compacting pressures and the sintering temperatures, the following influence of the multiplication of heating treatment on the structural restoration and performance improvement of sintered HVHSS specimens will be addressed later.

2.2 Processing (milling, granulation, compaction, and sintering)

The HVHSS with nearly full densification was achieved by the conventionally powder metallurgy sintering route, in which the milling, granulation, compaction, and sintering operations were involved with. The mixed powders were blended homogeneously by a wet ball milling process in a planetary mill for 240 min at a constant speed of 300 rpm, where zirconia (Ø 5 mm) was used as the ball mill material while the mill jar was zirconia as well, and anhydrous ethanol was selected as the media. The milled powders were then put into a vacuum drying oven and dried at a temperature of 80 °C for 6 h. The following process was to transform relatively fine powders into free-flowing granules that are ready to compress, namely granulation. The granules were then cold-pressed using the uniaxial compaction for 3 min, where ®20 Cylindrical Cr12MoV was used as the mold and the compaction pressure were set in the range of 100~400 MPa. The obtained green parts were consolidated by the non-pressure vacuum sintering process.

The sintering process was conducted in the heating furnace (Carbolite CWF 1200) with a vacuum of 10^{-1}~10^{-2} Pa; the sintering process is further depicted in Fig. 3b. Samples were firstly heated up to 450 °C at a rate of 15 °C/min and maintained for 15 min to eliminate the compaction lubricant of paraffin. They were continuously heated up to 1000 °C at a rate of 10 °C/min and maintained for 30 min. Subsequently, the sample was heated up to the designated sintering temperature at a rate of 10 °C/min and then maintained at targeted temperature with a duration of 60 min. Finally, the samples were cooled down to room temperature inside the furnace under the pressure of 10 Pa at the cooling rate of approximately 15 °C/min. The HVHSS samples sintered at 1150 °C, 1150 °C, 1175 °C, 1200 °C, 1225 °C, 1250 °C, and 1275 °C were respectively attained to get the evaluation of the effect of sintering temperature on the formability and performance of HVHSS specimen.

2.3 Mechanical and wear resistance assessments

The microhardness tests were carried out with a Micro-Vickers hardness tester. Eleven measurements were performed for each reported value. The load used was 500 g for 15 s, and the values were reported as HV500 units. The apparent fracture toughness was determined using the single-edge Notched Beam Method on a 10-ton capacity universal tester. The specimens were loaded in three-point bending at a crosshead speed of 0 .3mm/min according to ASTM E399.

Friction and wear behaviors of as-sintered HVHSS specimens were conducted on a pin-on-disc apparatus. An alumina ball of 6.35 mm with a Mosh hardness of 8.8 was slid against the sintered HVHSS discs. The sliding conditions were the applied load of 30 N, a reciprocating speed of 200 m/min with a stroke of 10 mm, and the sliding duration of 60 min. The wear loss was calculated from three repetitive tests by measuring the worn cross section to compare the wear resistance of HVHSS sintered at different temperatures.

2.4 Characterization

Densities were measured by the Archimedes' method according to according to ASTM C373-88. The relative density was calculated on the basis of the absolute density of specimens. After sintering, the size of sintered sample at different temperatures was measured with a digital caliper to calculate the shrinkage percentage. Morphological and compositional analyses were conducted by metallographic microscope and scanning electron microscopy (SEM) with energy-dispersive spectroscopy (EDS), where the samples were prepared by the mechanical polishing and etching with 4% Nital. The mean size of eutectic carbides was measured by the quantitative evaluation using the PhotoLib function. The structural transformation of the as-sintered HVHSS was analyzed by the X-ray diffractometry with Cu Kα radiation of $\lambda = 1.5406$ Å using a Ni filter and with a secondary graphite monochromator, where a scanning range of $2\theta = 20$~$80°$ with a step of 0.03° and 0.4 s was used. The phase identification was carried

out by comparing the experimental XRD patterns with the standard files compiled by the International Center for Diffraction Data (ICDD). STA449F3 Synchronous Thermal Analyzer was used to do the differential scanning calorimetric (DSC) analysis to quantify the weight loss, melting temperature, and possible reactions due to the endothermic/exothermic process; the sample (16 mg) in the alumina container was heated up to 1400 °C under the atmosphere of argon gas.

3 Results and discussion

3.1 Analysis of compacted HVHSS before sintering

The obtained granules were mostly round but irregular in shape as shown in Fig. 1a; their mean particle size was in the range of 75~100 μm suited for the compaction. From the view of microstructural analysis, it has been claimed that carbide networks were prone to form if pure metallic alloying elements were applied for the production of HVHSS, which undesirably undermined the plasticity and toughness of steel matrix. In this study, such Mo_2C, Cr_3C_2, and VC were directly selected as the pristine materials together with additional graphite and iron powders. After cold compaction, the specimen was analyzed by the XRD technique, as shown in Fig. 1b. It well demonstrated the mixed powders consisting of iron matrix and corresponding carbides including VC, Mo_2C, and Cr_3C_2, without any characteristic of graphite powder.

3.2 The compressibility assessment of compacted HVHSS before sintering

The compressibility of HVHSS specimen was characterized by the green density as the function of the applied compaction pressure in Fig. 2. Normally, the desirably green density could be achieved at a defined applied pressure [27]. The green parts could be reproducible and controllable using the PM fabrication, as shown by the inlet in Fig. 2. Seven compaction pressures were selected within the range of 100~400 MPa during the cold compacting operation. The results displayed the green density increased along with the increment of compaction pressure; the consolidated samples got a better attainment of sufficiently high densification due to increasing contacting area and the massive agglomerations of cemented carbide particles.

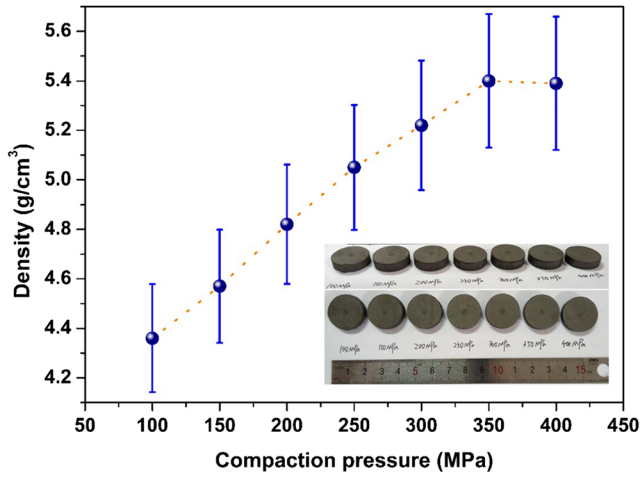

Fig. 2 Topography and corresponding density of the green HVHSS parts after cold compaction at different pressures

From 100 to 200 MPa, the powders tended to be brought close together, leading to the rearrangement of its displacement and the defects to be filled during compaction; the density as a result increased. As the pressure varied from 250 to 400 MPa, the powder constituents suffered deformation that was as the result of particle movement and orientation; the density continued to increase but grew up slowly in Fig. 2. It was noted that compaction pressure increased up to 350 MPa; the green density nearly kept the consistent trend with the sintered density and shrinkage rate as shown in Fig. 4. However, if the compaction pressure was lower, the sample peeled off easily. In the range of 250~400 MPa, the HVHSS specimen maintained good conformability, but some cracks appeared once the compacting pressure was 400 MPa, which

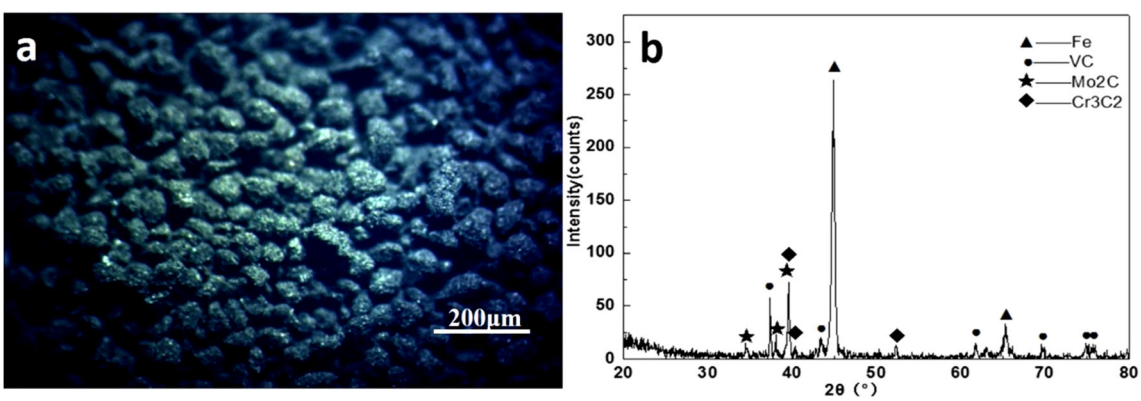

Fig. 1 Spherical morphology of mixed powders after granulation (**a**) and XRD pattern of mixed powders after wet milling process (**b**)

was due to bulk compression and involved with fracture or fragmentation of brittle powders [28]. In this case, the compaction pressure was 350 MPa for HVHSS fabrication with sufficiently high densification; the corresponding density and green density are around 5.3854 g/cm^3 and 7.6238 g/cm^3, respectively.

3.3 Sintering temperature determination for HVHSS

During the sintering process, the temperature must reach up to the solidus line where the liquid phase comes, whereas overheating in the contrast causes the rapid grain growth and formation of a continuous carbide network [29]. So the sintering temperature is the critical parameter to get the optimal volume of hardening carbide precipitations within the steel matrix. In order to assure the optimum temperature period of elimination of organic reagents and phase transformation during sintering process, thermal analysis by DSC was conducted to speculate the reactions during hot consolidation of greet bodies, as shown in Fig. 3a.

It is found in Fig. 3a that the weight loss at 400 °C is mainly due to the elimination of organic binder. As the heating increased up to around 830 °C, the peak corresponded to the transformation from ferrite to austenite. As the temperature reached up to 940 °C, the sample on the contrast gained the weight due to oxidation, which was associated with the specimen with relatively high surface area and some entrapped air. For example, vanadium carbides have the higher affinity with oxygen as high oxygen partial pressure exists [30, 31]. Not only is the vanadium-rich MC carbide oxidized, but also is the oxidation of fine Mo-rich M_2C carbides. This can be explained to be responsible for the weight increment.

When the temperature was over 1100 °C, the curve is diffused due to dissolution of carbides, indicating the beginning of sintering. Close to 1300 °C, the amount of liquid increased gradually due to melting of the austenitic phase and the carbides. During cooling process, the cooling temperature was relatively slow; thus, solidification of the liquid phase started with the MC carbide after appearance of a solid matrix (austenitic phase), formation of M_6C carbide, and then nucleation of the martensite phase (γ) which is favored by the high contents of alloying elements like V and Mo. Thus, the effect of the sintering temperature from 1100 to 1300 °C on the structural justification and performance optimization was mainly investigated in the following sintering process.

3.4 Density and shrinkage rates of sintered HVHSS

After compaction, the powders were in intimate contact with each other at points and some pores still existed among powders, or even large vacancies formed in some locations due to the irregular powder shapes [32]. The following sintering process turned the green bodies into a dense part. Figure 4 demonstrates the relative density and shrinkage rate of as-sintered HVHSS samples compressed at 350 MPa at different temperatures. With the increment of sintering temperature, the relative density and shrinkage rate rose. From 1150 to 1225 °C, the densification firstly increased and then became mediate, which was due to the solid sintering process [33]. In contrast, the relative density increased sharply when the temperature was from 1250 to 1300 °C, which could be attributed to very less porosity within HVHSS due to the coexistence of liquid plus solid sintering processes [34]; the relative density even reached up to 98.01% in Fig. 4, which was consistent with the weight loss in the DSC analysis (Fig. 3a). Note that the relative density and shrinkage rate increased continuously with the temperature increment from 1250 to 1275 °C. Since the sample sintered at 1250 °C still had a few pores, further heating facilitated improving diffusion and reaction among powders; the porosity would be less or even eliminated. However, the sintered HVHSS at 1300 °C displayed an irregular cylinder shape with the overmelted edge; the value of relative density was obtained, but it was difficult to calculate the shrinkage rate (thus not provided in Fig. 4).

The tendency of shrinkage rate was almost consistent with the change in relative density for HVHSS at different sintering

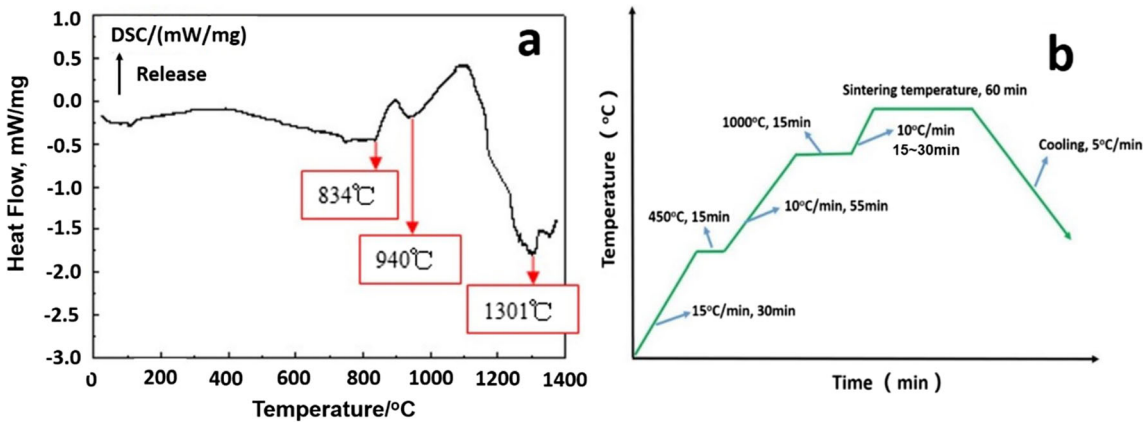

Fig. 3 Differential scanning calorimetry (DSC) curves (**a**) and schematic of detailed sintering processes for HVHSS (**b**)

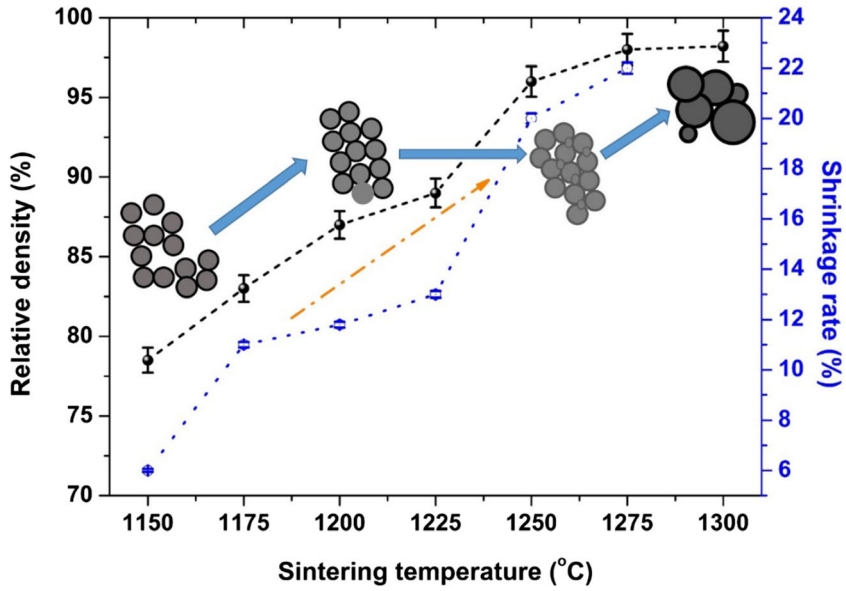

Fig. 4 Relative density and shrinkage rate of sintered HVHSS at different temperatures

temperatures, as shown in Fig. 4. A slight shrinkage of volume appeared as the temperature was less than 1225 °C, due to the solid sintering process. When the temperature was higher than 1225 °C, supersolidus liquid-phase sintering came up with the less porosities and a sharp increase in the volumetric contraction and thereby the shrinkage value, which was in good accordance with the DSC analysis in Fig. 3a. Those values indicated the phase transformation from single solid sintering to solid consolidation together with liquid sintering. The increasing shrinkage from 1250 to 1275 °C further elucidated that the sample at 1250 °C still had a few pores; further increment of temperature led to as-sintered compact more densified. However, the liquid-phase volume fraction will be increased with the sintering temperature increase. Sintering temperature of 1300 °C conversely probably produced excessive liquid and resulted in the distortion of part; the overmelted appearance even occurred in this case. These values allowed to get a better attainment of the sintered HVHSS samples with full density at the temperature of 1250–1275 °C.

The values in relative density and shrinkage at different sintering temperatures in Fig. 4, together with the DSC analysis of HVHSS in Fig. 3a, well indicate sequential occurrence of binder elimination, transformation from ferrite to austenite and formation of principle carbides accompanied by excessive liquid-phase formation. Also, the increasing sintering temperatures facilitated the matrix densification followed by less pores.

3.5 Structural analysis of sintered HVHSS

Figure 5 shows the microstructural evolution of as-sintered HVHSS samples at the temperatures of 1150 °C, 1175 °C, 1200 °C, 1225 °C, 1250 °C, 1275 °C, and 1300 °C, respectively. The results well affirmed that the studied HVHSS consists of dominant austenite (A) and martensite (M), with amount of α-Fe matrix and two primary types of carbide precipitations (MC and M_6C) in Fig. 5. As compared to the pristine mixed powders in Fig. 1, such peaks associated with Mo_2C and Cr_3C_2 disappeared while vanadium carbide was more distinguishable, which was explained to be due to the dissolution of alloying carbides and carbon into austenite when the sintering temperature was sufficiently high temperature. The XRD patterns further justified the grain growth and increasing concentration of carbides by the enlarging diffraction peaks corresponding to the precipitated MC and M_6C type carbides. It was noticeable that the major diffraction peaks corresponding to MC and M_6C phases at 1275 °C were more intensive than that at 1250 °C. Further, as the sintering temperature went higher, the intensified M and A components are observed in Fig. 5. Nevertheless, excessive amount of

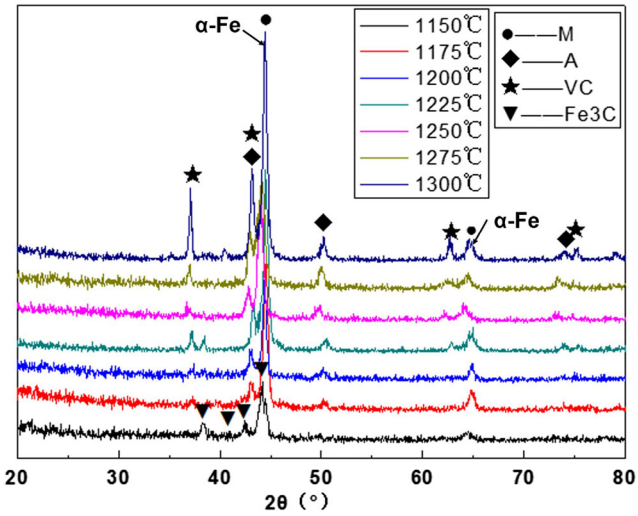

Fig. 5 XRD patterns of sintered HVHSS specimen at different temperatures

austenite (A) conversely undermined the mechanical capability of HVHSS as shown in Fig. 8. In addition, M_6C type was preferentially dissolved within the ferrous matrix, which was hardly distinguished from the MC, which was ascribed to the nucleation of the M_6C carbide at the MC/austenite interface and the MC carbide inside the M_6C carbide or at the MC/M_6C interface [28]. At the relatively lower sintering temperature of 1150 °C, trace of cementite is found in Fig. 5, which was due to the eutectic solidification of iron together with carbon according to metastable Fe–C phase diagram.

The optically metallurgic microscopy of HVHSS well further revealed the improved densification with no significant porosity among the sintered HVHSS specimens in Fig. 6. It could be observed that the grain size was gradually increased with the increment of the sintering temperature. However, as the temperature further increased, matrix and carbide coarsening took place. In the range of 1150–1200 °C, processes of segregation and solidification were presented, due to the solid phase dissolution in the structure. Thus, the carbide phase was highly dispersed within the matrix without the distinct increase in the carbide size, but the densified degree increased continuously in Fig. 4. At 1225 °C, the eutectics phases appeared as shown in Fig. 6d. The M_6C and MC carbides mainly retained the globular morphologies along the grain boundaries throughout HVHSS, without a skeleton-type eutectic surrounding the ferrite grains or carbides coarsening. However, the XRD patterns with the characteristic of the narrowing peaks are observed in Fig. 5, which indicated the liquid-phase reactions occurring during the sintering. The comparison of the optical images well revealed that relatively homogeneous dispersion and finer grains happened at 1250 °C in Fig. 6e. The liquifying process continued at 1275 °C was accompanied by the perceivable carbides that coalesce; more liquid phase came, and crystallite grains began to engulf adjacent crystal grains in Fig. 6f. However, large blocky carbide grains appeared at the grain boundaries as the sintering temperature further increased to 1300 °C; the carbide grain growth is observed obviously in Fig. 6g. As a result, the deterioration of mechanical properties is found in Fig. 8, due to more weakening action of the carbide networks.

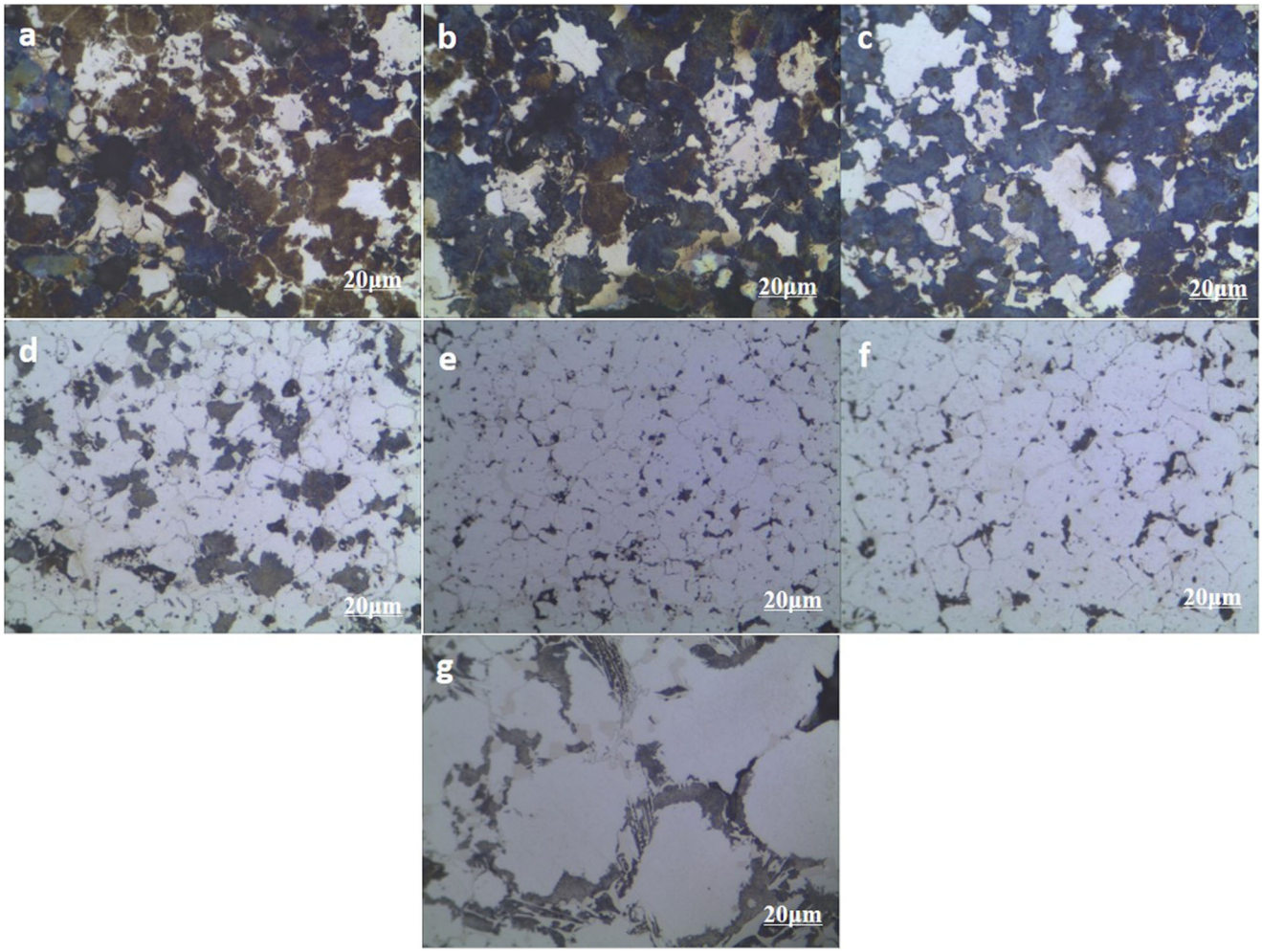

Fig. 6 Optical observation of sintered HVHSS at different sintering temperatures. **a** 1150 °C. **b** 1175 °C. **c** 1200 °C. **d** 1225 °C. **e** 1250 °C. **f** 1275 °C. **g** 1300 °C

The eutectic carbides could be further identified by the SEM/EDS analysis. Figure 7 shows the microscopic observation of sintered HVHSS specimen at 1275 °C. As the sintering temperature was at 1275 °C, both as-rounded carbide particles within the grains and as-angular or continuous carbides at the grain boundary of prior austenite are shown in Fig. 7. The vanadium carbides could be distinguished from the matrix easily as shown by the green color coded in the EDS mapping, which well elucidated the gray intercellular or interdendritic phases with high amount of vanadium carbides in the SEM. The EDS qualitative analysis further showed intense characteristic peaks pertaining to M and A at A and D locations, while higher quantities of vanadium carbides have been recorded in the B and C locations. There obtained a distinct contrast between the underlying ferrous matrix and VC inclusions. The EDS-mapping analysis further clarified the distribution of iron, chromium, molybdenum, and vanadium within as-sintered HVHSS matrix. It was found that there was a strong signal of vanadium and a slightly weak signal for Mo and Cr along with the vanadium carbide distribution; vanadium carbide was overlapped with the molybdenum and chromium carbides. It is clear therefore that carbides (e.g., chromium, molybdenum, and vanadium) had high solubility within austenite, while complex carbide gradually precipitated in the ferrite.

With the sintering temperature increasing, grain coarsens and carbides were preferentially moved to the interfaces and/or recombined with the surrounding carbide components and iron matrix. Such Mo_2C carbide preferred to be M_6C and VC would be transformed into MC, while chromium carbide tended to form the interstitial phases with the involvement of Fe [35]. Such carbide either was situated inside grain or was entrapped in grain boundaries, as affirmed in Fig. 7. It could be concluded that vanadium carbide presenting as the particulates were dispersed within the ferrous matrix while Mo and Cr carbides were dissolvable into the ferrous matrix.

3.6 Mechanical and tribological assessments

The values of mechanical hardness and bending strength for as-sintered HVHSS at different temperatures are shown in Fig. 8. It could be found that for the sintering processes conducted at 1150 °C, the hardness was no more than 200 HV. As the sintering temperature rose, an increase of the hardness reaching more than 850 HV at 1275 °C happened. However, when the sintering temperature further increased to 1300 °C,

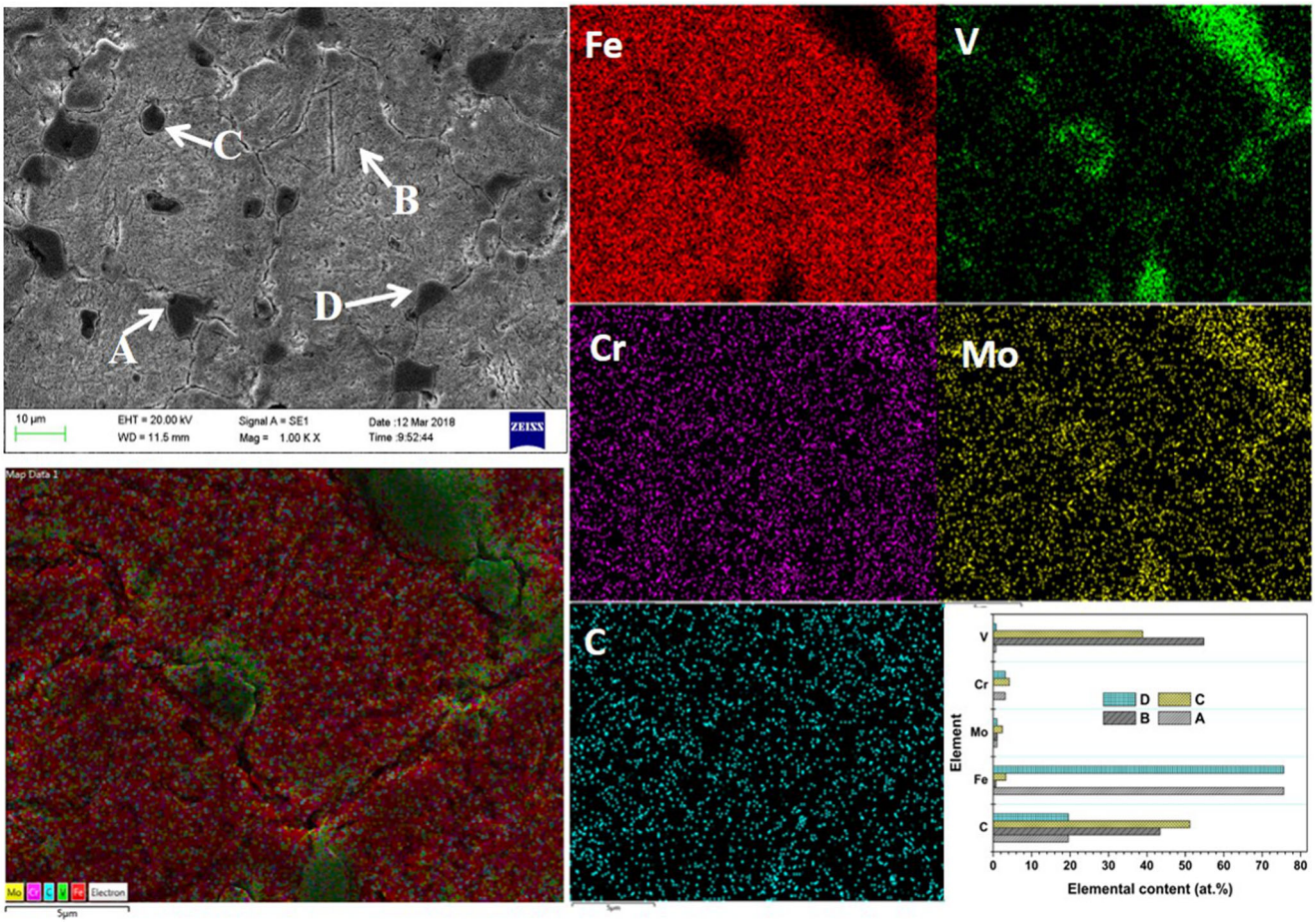

Fig. 7 SEM observation and corresponding EDS-mapping analysis of sintered HVHSS at 1275 °C

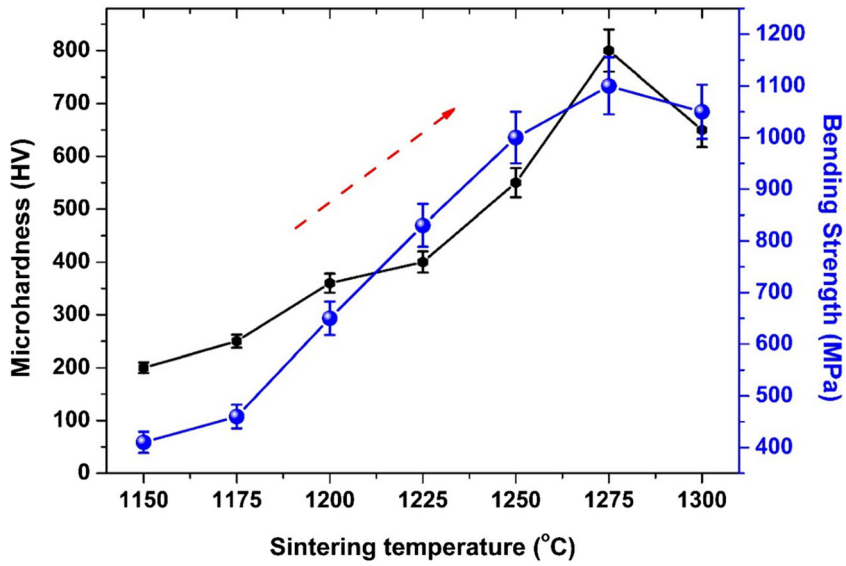

Fig. 8 Resultant hardness and bending strength of sintered HVHSS at different sintering temperatures

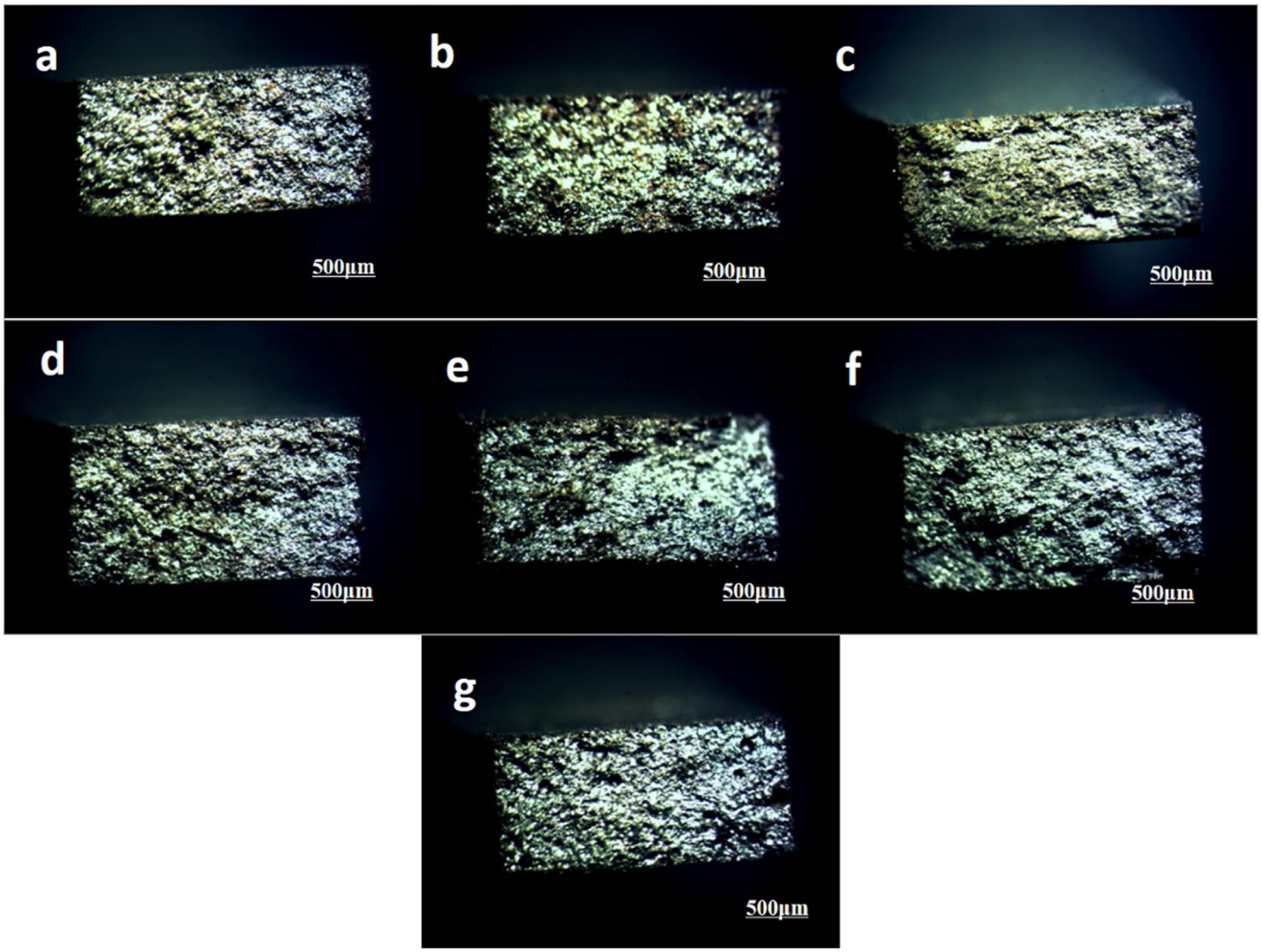

Fig. 9 Fractured morphological observation of sintered HVHSS at different temperatures. **a** 1150 °C. **b** 1175 °C. **c** 1200 °C. **d** 1225 °C. **e** 1250 °C. **f**1275 °C. **g**1300 °C

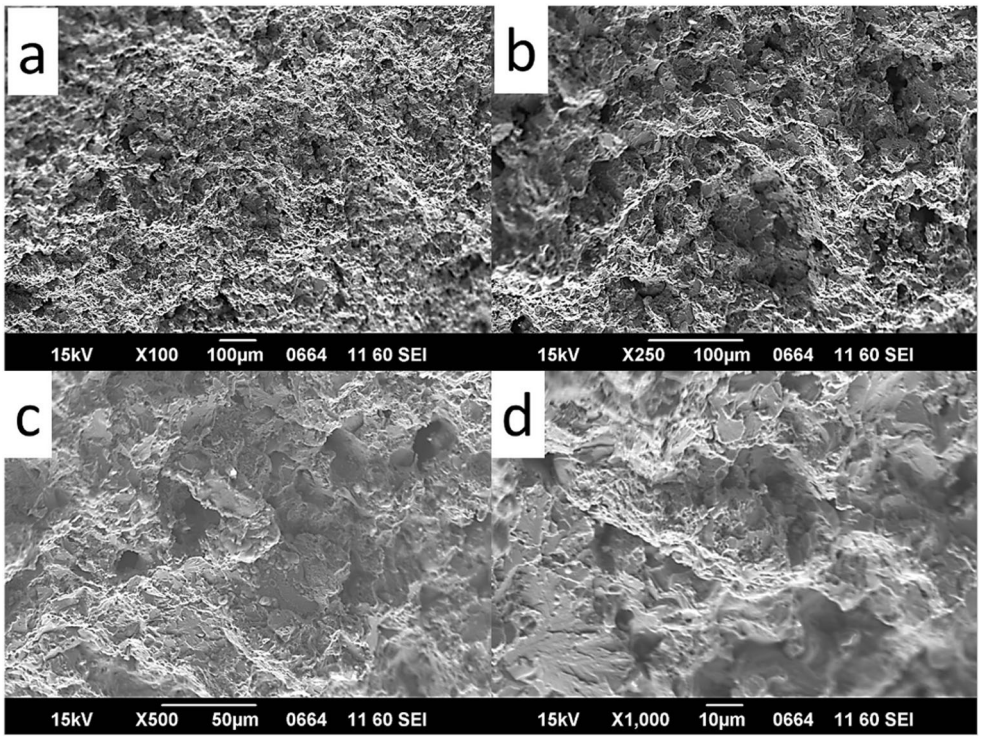

Fig. 10 General view of the fracture surface (**a**), transgranular brittle fracture zone (**b**), ductile dimpled fracture (**c**, **d**) of HVHSS sample sintered at 1275 °C

pores were probably eliminated; the mechanical strength instead became worse due to excessively large grain size [36, 37], as shown in Fig. 8. This was consistent with the observation of excessive growth of grain in Fig. 6g.

The bending strength of HVHSS displayed the similar tendency with the increment of sintering temperature, which was a typical evaluation of bulk toughness. It was noticeable that HVHSS demonstrated the poor bending strength at the sintering temperature of 1150 °C, around 400 MPa; the rise of sintering temperature helped enhancing the bending strength, and a maximum value of 1100 MPa came at 1275 °C in Fig. 8. On the basis of Fig. 4, the increased densification and less porosity within the matrix contributed significantly to the improvement in mechanical properties of HVHSS. In contrast, the decrease in the bending strength became accentuated for the continuous increment of sintering temperature to 1300 °C. These happenings were closely associated with the structural restoration during sintering in terms of MC carbide/matrix interface and the balanced austenite and martensite phase, e.g., carbide morphology and distribution [38, 39]. For example, the intensified diffraction

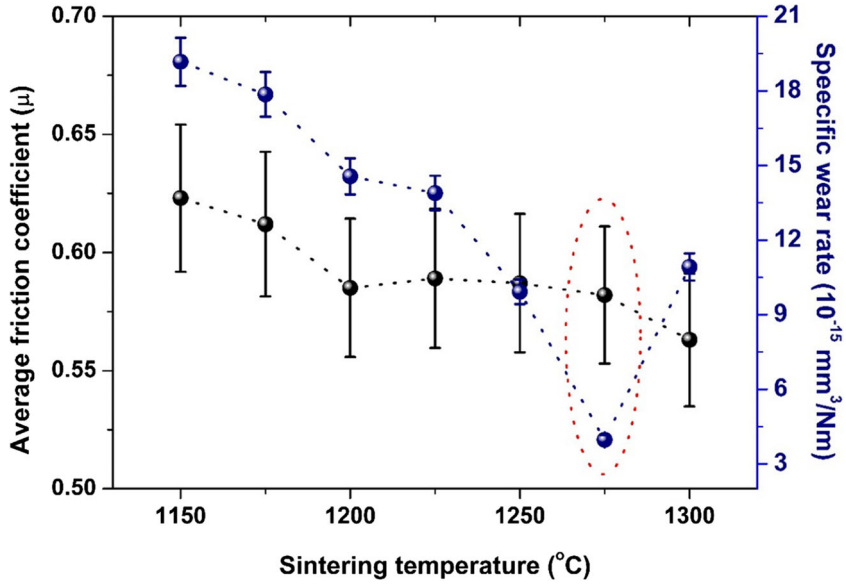

Fig. 11 Friction and wear variations of HVHSS specimen as the function of sintering temperatures

peaks corresponding to the martensite phase and eutectic carbides contributed to the weakened strength and toughness as shown in Fig. 5.

Generally, the fracture initially occurred after cracking between brittle carbides and martensite matrix that would create subcritical cracks; once the growing crack exceeded the critical length, failure of HSS definitely took place with the sudden brittle fracture [40]. The improved mechanical performance of sintered HVHSS dominantly depended on the microstructure transformation, smaller grain size, and more uniform and finer distribution of primary carbides. The mechanical capability of HVHSS was optimum as the sintering temperature was 1275 °C in this study. The following optical observation of fractured HVHSS well showed all fractured surface with no appreciable plastic deformation in Fig. 9. Looking at the fracture surface with a SEM, there are two key features, a large quantity of dimples and microvoid coalescence as shown in Fig. 10, which well indicated the cooccurrence of ductile and brittle fracture for sintered HVHSS at 1275 °C. In the case of microvoid formation in HVHSS, these voids are closely associated with microscopic contaminants within HSS matrix, e.g., entrapped gaseous media [41]. Particle cracking or interfacial failure between precipitate particles and the matrix is reported to be mainly responsible for this fracturing process of HVHSS specimen at 1275 °C [42, 43]. Thus, the further quenching and annealing process were required to refine globular particles to lower brittleness and suppress crack propagation [44], thus improving the strength and toughness of sintered HVHSS.

Appreciable sintering temperature promoted densification and more transformation of retained austenite into martensite, which led to the improved mechanical capability of bulk HVHSS associated with the hard-yet-tough nature, consequently inhibiting wear and stabilizing friction [45, 46]. Figure 11 shows the variations of friction and wear behavior of the sintered HVHSS samples at different temperatures. Friction results revealed the average coefficient of friction against alumina ball in the range of 0.55~0.65. As the sintering temperature increased, HVHSS was more densified to promote the sliding stability during friction evaluation. The lowering friction was closely associated with relatively higher inclusion of vanadium carbide within HSS that delivered the benefits of lowering friction. At the stressed shearing contacts in air, tribo-induced reactions facilitated the phase transformation from carbide into oxides, which was assumed to be the contribution of friction reduction. In particular, the vanadium oxide has the inherent structure composed of multiple V_2O_5 layers stacked via van der Waals force and makes itself available as the solid lubricants, which facilitate improving the frictional stability due to the crystallographic slip attribute [19]. Thus, sufficiently, high inclusion of vanadium carbide is beneficial to lower friction.

As for the wear of as-sintered HVHSS, it was primarily attributed to the large amount of reinforcing carbide particles that act as obstacle against abrasive and adhesive wear. Though wear and friction assessment of sintered HVHSS were conducted at room temperatures, still desirable capability of HSS with high vanadium was achieved as expected. However, HVHSS specimen was overheated by as little as 5 °C; rapid grain growth and formation of a continuous carbide network occurred, which as a result damaged the comprehensively mechanical capability of bulk [14, 37]. Thus, wear increment took place at the sintering temperature of 1300 °C as shown in Fig. 10. In this study, apart from high inclusion of vanadium carbide, balanced formation of complex carbides and martensitic microstructure contributed to the desired strength and toughness and the consequent improvement in wear prevention at the sintering temperature of 1275 °C."

4 Conclusion

In this work, direct production of HVHSS was achieved by the conventionally powder metallurgical processing including cold compaction and controlled sintering. The alloying process with the direct use of hardening carbide demonstrates the superiority of fabrication of high strength high-speed steel products that are potentially used for hot rolling sector. HVHSS retained the desirable structure and mechanical capability and enabled friction reduction and wear mitigation highly depends on the sintering temperatures. Chromium carbide Cr_7C_3 and Mo_2C were dissolved within ferrous matrix, while grain size and distribution of vanadium carbides varied with the sintering temperatures. The samples sintered at 1275 °C demonstrated the optimal mechanical and tribological capabilities, which could be associated with not only the physical aspects including sufficient densification and carbide grain not too coarse as well as relatively uniform dispersion but also higher amount of vanadium carbide that makes significant contribution to the improved refinement of more hardening precipitates with the martensitic structure. On the basis of the existing results obtained so far, future work is proposed for the integrated strategies of tempering and annealing to optimize the toughness and strength of HVHSS.

Originality statement We confirm that the article is original without consideration for publication elsewhere, and the article has not been published previously. The article has been written by the stated authors who have read and approve this version of the article.

Author contributions Experiments and mechanical assessments were performed by Huan Li; Shanhong Wan was responsible for analyzing the structural results and composing the paper. Hongtao Zhu, Kiet Tieu, and Qi Xue contributed to design of experiments.

Funding information The work was also supported by the Undergraduate Innovation and Entrepreneurship Program in Si Chuan province (No. KSZ14122). The work is also funded by Australian Research Council (ARC) Discovery Project (DP) 150103718.

Compliance with ethical standards

Conflict of interest The authors declare that they have no conflict of interest.

References

1. Hoyle G (2013) Recent developments in high-speed steels. Int Metall Rev 9:49–91
2. Pellizzari M, Cescato D, De. Flora MG (2009) Hot friction and wear behaviour of high speed steel and high chromium iron for rolls. Wear 267:467–475
3. Garza-Montes-de-Oca NF, Rainforth WM (2009) Wear mechanisms experienced by a work roll grade high speed steel under different environmental conditions. Wear 267:441–448
4. Chaus AS, Hudáková M (2009) Wear resistance of high-speed steels and cutting performance of tool related to structural factors. Wear 267:1051–1055
5. Mirjavadi SS, Alipour M, Emamian S, Kord S, Hamouda AMS, Koppad PG, Keshavamurthy R (2017) Influence of TiO2 nanoparticles incorporation to friction stir welded 5083 aluminum alloy on the microstructure, mechanical properties and wear resistance. J Alloys Compd 712:795–803
6. Mirjavadi SS, Alipour M, Mamouda AMS et al (2014) Investigation of the effect of Al-8B master alloy and strain-induced melt activation process on dry sliding wear behaviour of an Al-Zn-Mg-Cu alloy. Mater Des 53:308–316
7. Mirjavadi SS, Alipour M, Mamouda AMS et al (2014) Effect of multi-pass friction stir processing on the microstructure, mechanical and wear properties of AA5083/ZrO2 nanocomposites. J Alloys Compd 726:1262–1273
8. Ebrahimi M, Zarei-Hanzaki A, Abedi HR, Azimi M, Mirjavadi SS (2017) Correlating the microstructure to mechanical properties and wear behaviour of an accumulative back extruded Al-Mg_2Si in-situ composite. Tribol Int 115:199–211
9. Alipour M, Mirjavadi S, Besharati Givi MK et al (2012) Effects of Al-5TI-1B master alloy and heat treatment on the microstructure and dry sliding wear behavior of an Al-12Zn-3Mg-2.5 Cu alloy. Iran J Mater Sci Eng 9:8–16
10. Chaus AS (2008) On the wear resistance of high-speed steels. J Frict Wear 29:24–34
11. AlMangour B, Grzesiak D, Yang J–M (2016) Nanocrystalline TiC-reinforced H13 steel matrix nanocomposite fabricated by selective laser melting. Mater Des 96:150–161
12. AlMangour B, Cescato D, Yang J–M (2017) Selective laser melting of TiB2/H13 steel nanocomposites: influence of hot isostatic pressing post-treatment. J Mater Process Technol 244:344–353
13. Bressan JD, Hesse R, Silva EM Jr (2001) Abrasive wear behaviour of high speed steel and hard metal coated with TiAlN and TiCN. Wear 250:561–568
14. García C, Romero A, Herranz G, Blanco Y, Martin F (2016) Effect of vanadium carbide on dry sliding wear behaviour of powder metallurgy AISI M2 high speed steel processed by concentrated solar energy. Mater Charact:175–186
15. Godec M, Bati B, Mandrino D, Nagode A et al (2010) Characterization of the carbides and the martensite phase in powder-metallurgy high-speed steel. Mater Charact 61:452–458
16. Serna MM, Jesus ERB, Galego E, Martinez LG, Corrêa HPS, Rossi JL (2006) An overview of the microstructures present in high-speed steel-carbide crystallography. Mater Sci Forum 530-531:48–52
17. Hossain R, Pahlevani F, Quadir MZ, Sajajwalla V (2016) Stability of retained austenite in high carbon steel under compressive stress: an investigation from macro to nano scale. Sci Rep 6:34958
18. Zhong LS, Ye FX, Xu YH, Li JS (2014) Microstructure and abrasive wear characteristics of in-situ vanadium carbide particulate-reinforced iron matrix composites. Mater Des 54:564–569
19. Fateh N, Fontalvo G, Mitterer C (2008) Tribological properties of reactive magnetron sputtered V2O5 and VN–V2O5 coatings. Tribol Lett 30(1):21–26
20. Wei SZ, Zhu JH, Xu LJ, Long R (2006) Effects of carbon on microstructure and properties of high vanadium high-speed steel. Mater Des 27(1):58–63
21. Mascarenhas J (1997) Sintering behaviour, microstructure and mechanical properties of vanadium enriched high speed steels processed in vacuum-and nitrogen rich atmospheres, Thesis, University of Bradford
22. Nilsson M, Olsson M (2013) An investigation of worn work roll materials used in the finishing stands of the hot strip mill for steel rolling. Proc Inst Mech Eng J 227(8):837–844
23. Singh K, Khatirkar RK, Sapate SG (2015) Microstructure evolution and abrasive wear behaviour of D2 steel. Wear 328-329:206–216
24. Ezugwu EO, Lai CJ (1995) Failure modes and wear mechanisms of M35 high speed steel drills when machining Inconel 901. J Mater Process Technol 49:295–312
25. Straffelini G, Benedetti M, Fontanari V (2014) Damage evolution in sinter-hardening powder-metallurgy steels during tensile and fatigue loading. Mater Des 61:101–108
26. Pan FS, Wang WQ, Tang AT, Wu LZ et al (2011) Phase transformation refinement of coarse primary carbides in M2 high speed steel. Pro Nat Sci: Mater Int 21:180–186
27. Romano P, Velasco FJ, Torralba JM, Candela N (2006) Processing of M2 powder metallurgy high-speed steel by means of starch consolidation. Mater Sci Eng A 419:1–7
28. Eroglu S (2010) Sintering and mechanical properties of AISI M2 high speed steel powder molded at low pressures. Mater Manuf Process 25(9):1025–1029
29. Gimnez S, Zubizarreta C, Trabadelo V, Iturriza I (2008) Sintering behaviour and microstructure development of T42 powder metallurgy high speed steel under different processing conditions. Mater Sci Eng A 480:130–137
30. Santafé C, Borgianni C (1975) Study of the oxidation kinetics of vanadium carbide. Oxid Met 9:415–425
31. Zhu Q, Zhu HT, Tieu AK, Kong C (2011) Three dimensional microstructure study of oxide scale formed on a high-speed steel by means of SEM, FIB and TEM. Corros Sci 53:3603–3611
32. Peng HL, Hu L, Li LJ, Zhang LY, Zhang XL (2018) Evolution of the microstructure and mechanical properties of powder metallurgical high-speed steel S390 after heat treatment. J Alloys Compd 740:766–773
33. Liu ZY, Loh NH, Khor KA, Tor SB (2000) Microstructure evolution during sintering of injection molded M2 high speed steel. Mater Sci Eng A 293:46–55
34. Tjong SC, Ma ZY (2000) Microstructural and mechanical characteristics of in-situ metal matrix composites. Mater Sci Eng R Rep 29:49–113
35. Rong W, Andrén HO, Wisell H, Dunlop GL (1992) The role of alloy composition in the precipitation behaviour of high speed steels. Acta Metall Mater 40(7):1727–1738
36. Zhang QK, Jiang Y, Shen WJ, Zhang HB, He YH, Lin N et al (2016) Direct fabrication of high-performance high speed steel products enhanced by LaB6. Mater Des 112:469–478
37. Mahesh K, Sankaran S, Venugopal P (2012) Microstructural characterization and mechanical properties of powder metallurgy dual phase steel preforms. J Mater Sci Technol 28(12):1085–1094
38. Zheng YX, Wang FM, Li CR, Li YL, Cheng J, Cao RF (2018) Effect of microstructure and precipitates on mechanical properties of Cr-Mo-V alloy steel with different austenitizing temperatures. ISIJ Int 58:1126–1135

39. Yang ZQ, Liu ZD, He XK, Qiao SB, Xie CS (2018) Effect of microstructure on the impact toughness and temper embrittlement of SA508Gr.4N steel for advanced pressure vessel materials. Sci Rep 8:207
40. Iqbal A, King JE (1990) The role of primary carbides in fatigue crack propagation in aeroengine bearing steels. Int J Fatigue 12: 234–244
41. Kim CK, Park JI, Lee S, Kim YC et al (2005) Effects of alloying elements on microstructure, hardness, and fracture toughness of centrifugally cast high speed steel rolls. Metall Mater Trans A 36: 87–97
42. Kumar S, Curtin WA (2007) Crack interaction with microstructure. Materialstoday 10:34–44
43. Chawla N, Shen Y-L (2001) Mechanical behavior of particle reinforced metal matrix composites. Adv Eng Mater 3:357–370
44. Abrão AM, Denkena B, Köhler J, Breidenstein B, Mörke T, Rodrigues PCM (2014) The influence of heat treatment and deep rolling on the mechanical properties and integrity of AISI 1060 Steel. J Mater Process Technol 214:3020–3030
45. Budin S, Jaafar TR, Selamat MA (2016) Microstructure and mechanical properties of high speed steel with addition of ferrophosphorus on sintering temperature. AIP Conference Proceedings 1774:060002
46. Wei SZ, Zhu JH, Xu LJ, Long R (2005) The study on abrasive wear of carbon of high vanadium high speed steel compared with that of high chromium cast iron. ASME Proc: Wear and Fatigue Mater WTC2005–63590:105–106

Publisher's note Springer Nature remains neutral with regard to jurisdictional claims in published maps and institutional affiliations.